

THE QUADRUPLE SYSTEM HIP 45734

ANDREI TOKOVININ

Cerro Tololo Inter-American Observatory,* Casilla 603, La Serena, Chile
 Draft version January 27, 2020

ABSTRACT

HIP 45734 is a quadruple system of 2+2 architecture located at 68 pc from the Sun. The outer 9'' system A,B has a period of $\sim 10^4$ yr. The subsystem Aa,Ab is a visual binary with a period of 20.1 years and an eccentricity of 0.78. Its periastron in 2019.1 was observed spectroscopically, yielding masses (1.10 ± 0.04 and $0.98 \pm 0.03 M_{\odot}$) and orbital parallax, 14.90 ± 0.37 mas. The masses, luminosities, and colors approximately agree with evolutionary models of main sequence stars. The component Aa has a detectable lithium line, whereas in Ab it is absent. The pair Ba,Bb is a single-lined spectroscopic binary with a period of 0.5552 day and an orbital inclination of $\sim 45^{\circ}$ derived by modeling the rotationally broadened line profile with “flat bottom”. The mass of Bb is $\sim 0.4 M_{\odot}$. The star B is chromospherically active (an x-ray source); its flux is modulated with the orbital period by starspots, in addition to occasional flares. The system is probably older than ~ 600 Myr; it does not belong to any known moving group.

Keywords:

1. INTRODUCTION

Discovery of a population of young chromospherically active stars in the solar neighborhood by their x-ray radiation in the 1980s and 1990s stimulated follow-up observations to determine their physical parameters, ages, rotation, kinematics, etc. Many of these stars belong to young moving groups and associations (Torres et al. 2006). However, a large fraction (40%) are old short-period binaries (Makarov 2003). Recently renewed interest in nearby young stars is stemmed by the search for exoplanets using high-contrast imagers because young self-luminous planets are easier to detect compared to their older and cooler counterparts (e.g., Asensio-Torres et al. 2018).

The object of this note is a 9'' visual binary discovered by J. Herschel in 1837 and known as HJ 4214. Its secondary component B is called a “T Tau-type Star” (Torres et al. 2006), probably because, apart from being chromospherically active, the stars are located in the sky close to the Chamaleon star forming region. However, the distance, the fast proper motion (PM), and the radial velocity (RV) make it clear that this pair is unrelated to the molecular cloud and only projects onto it. Common identifications and main parameters of the two visual components A and B are given in Table 1. The *Gaia* astrometry of the star A is affected by its acceleration, leading to a larger parallax error compared to the star B. The *V* magnitudes in Table 1 are calculated from the *Gaia* DR2 photometry using the prescription given on its web site.¹ The *Tycho* photometry gives 8.41 and 9.66 mag for A and B, both fainter compared to *Gaia*. Simbad gives for A the *V* magnitude of the combined light of A and B, 8.05 mag.

These stars, believed to be pre-main sequence (PMS),

Table 1
 Main Parameters of HIP 45734

Parameter	A	B
WDS Identifiers	J09194–7739, HIP 45734, HD 81485	HJ 4214, KOH 83, TYC 9399-2452-1, RX J0919.4-7738
PM (mas yr ⁻¹)	–106.8, 68.5	–107.9, 70.8
Parallax (mas) ^a	14.53 ± 0.15	14.66 ± 0.03
Spectral type	G7V	K0IVe
<i>V</i> (mag)	8.31	9.44
<i>G</i> (mag)	8.17	9.24
<i>K</i> (mag)	6.78	7.44
RV (km s ⁻¹)	4.9	7.7

^b Proper motion and parallax are from the *Gaia* DR2 (Gaia collaboration 2018).

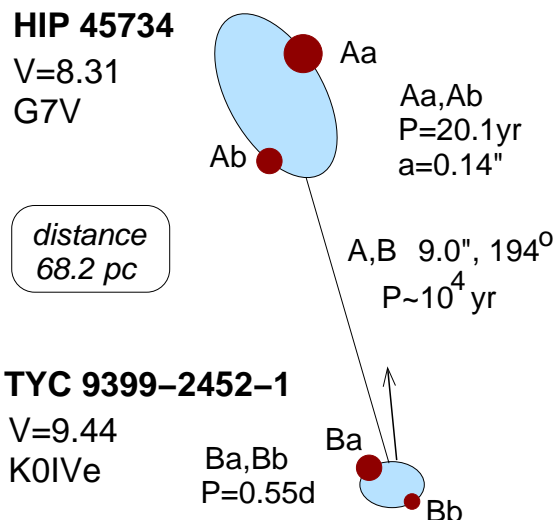


Figure 1. Architecture of the HIP 45734 quadruple system (not to scale).

are featured in the large survey of Torres et al. (2006). The equivalent width (EW) of the lithium line in A

*National Science Foundation’s National Optical-Infrared Astronomy Research Laboratory
 Electronic address: atokovin@ctio.noao.edu

¹ See Chapter 5.3.7 of *Gaia* DR2 documentation at <https://gea.esac.esa.int/archive/documentation/GDR2/>.

Table 2
Parameters of the CCF profiles

Parameter	Aa	Ab	B
Amplitude	0.242	0.161	0.053
σ (km s ⁻¹)	4.28	4.07	38.7
Amplitude \times σ (km s ⁻¹)	1.03	0.66	2.05
$V \sin i$ (km s ⁻¹)	4.7	4.0	67.4

and B was measured at 0.06 and 0.05 Å, respectively. Covino et al. (1997) took spectra of HIP 45734 together with other presumably young stars in Chamaeleon with a resolution of 10,000. They confirmed presence of the lithium line and noted that the southern star B has emissions in the H α , helium 5876 Å and sodium D lines. Broad lines of the star B resembled a blend, making Covino et al. think that B is a double-lined spectroscopic binary. However, no follow-up observations were conducted to determine the orbit. Desidera et al. (2006) also took high-resolution spectra of both visual components. They have not seen B as double-lined, but confirmed the strong H α emission in its spectrum and its very high chromospheric activity index; the H α emission in A was “much lower”. Thinking that B is a double-lined binary, Asensio-Torres et al. (2018) looked for low-mass companions around it using high-contrast adaptive optics, but found only a faint background source at 4''3 separation.

The star A was resolved by Koehler (2001) into a close binary. Its first visual orbit with a period of 19.8 yr was computed by Tokovinin et al. (2015). My interest in this quadruple system is twofold. First, it belongs to the sample of solar-type stars within 67 pc (Tokovinin 2014), although the *Gaia* parallax now puts it just outside its distance limit. Spectroscopic observations were conducted to determine the unknown period of Ba,Bb, complementing the multiplicity statistics in this sample. On the other hand, the orbit of the interferometric pair Aa,Ab offered the prospect of measuring masses of young, possibly PMS, stars to test stellar evolutionary models. Both goals are now reached and make the subject of this paper.

Figure 1 illustrates the architecture of this quadruple system according to this study. The pair Aa,Ab is a visual binary with an eccentric 20.1 yr orbit. It is composed of normal and apparently inactive dwarfs with masses of 1.12 and 1.0 M_{\odot} . In contrast, Ba,Bb is a close spectroscopic binary with a period of only 0.55 day. The star Ba, similar in mass to Ab, has a fast axial rotation synchronized with the orbit. Naturally, it is also highly active. The mass of the spectroscopic secondary Bb is about 0.4 M_{\odot} . Despite the short period, this pair is not in contact; it is not eclipsing owing to the large inclination.

Observational data and methods are recalled briefly in Section 2. Then in Sections 3 and 4 the orbits of both inner subsystems are given; the outer orbit is discussed in Section 5. Section 6 matches stellar parameter to the evolutionary models. A short discussion in Section 7 closes the paper.

2. OBSERVATIONAL DATA

High-resolution ($R \sim 80,000$) spectra of the components A and B (10 and 15, respectively) were taken with the CHIRON optical echelle spectrometer

Table 3
Combined Orbit of Aa,Ab

Parameter	Value
Period P (yr)	20.10 \pm 0.29
Periastron T_0 (yr)	2019.103 \pm 0.004
Eccentricity e	0.7818 \pm 0.0038
Semimajor axis a (arcsec)	0.1405 \pm 0.0019
Node Ω (deg)	21.6 \pm 0.7
Longitude ω (deg)	276.3 \pm 0.3
Inclination i (degr)	63.0 \pm 0.6
Primary amplitude K_1 (km s ⁻¹)	9.420 \pm 0.042
Secondary amplitude K_2 (km s ⁻¹)	10.537 \pm 0.073
γ velocity (km s ⁻¹)	4.813 \pm 0.029
R.M.S. residuals (km s ⁻¹)	0.05, 0.17
M_{Aa} (M_{\odot})	1.12 \pm 0.04
M_{Ab} (M_{\odot})	1.00 \pm 0.03

(Tokovinin et al. 2013) in 2015 (Tokovinin 2015) and in 2018–2019, in the service mode. They cover the wavelength range from 415 nm to 880 nm in 53 orders. The spectrograph is fiber-fed by the 1.5 m telescope operated by Small & Moderate Aperture Research Telescope System (SMARTS) Consortium.² The data analysis closely follows previous work (Tokovinin 2016a). A cross-correlation function (CCF) of the reduced spectrum with a binary mask using lines in the range from 450 nm to 650 nm allows us to measure the RV and to estimate other parameters such as the line width and the related projected axial rotation $V \sin i$. Average parameters of the Gaussian functions that approximate the CCFs are listed in Table 2. The rotational velocities were deduced from the width of the CCF dips for Aa and Ab and determined in Section 4.3 for B. The RVs and their residuals from the orbits are given below.

The CHIRON spectra show no emissions in the Balmer lines of the component A, while these lines in the component B are practically absent, being completely filled by emission. No other emission lines are detectable in either component.

The positional measurements of the pair Aa,Ab used for the calculation of its combined orbit are, mostly, made by the speckle camera at the 4.1 m Southern Astrophysical Research (SOAR) telescope. The instrument and data processing are described by Tokovinin (2018). The latest series of measurements and references to prior publications can be found in Tokovinin et al. (2019). The Washington Double Star Catalog (WDS, Mason et al. 2001) was consulted for the published measurements of the outer and inner resolved pairs. Since the first orbit of Aa,Ab was computed in 2014, 10 new speckle measurements covering the periastron have been made.

As in the previous papers of this series, orbital elements and their errors were determined by the least-squares fits with weights inversely proportional to the square of adopted errors. The IDL code `orbit`³ was used (Tokovinin 2016b).

3. SUBSYSTEM AA,AB

The pair Aa,Ab was first resolved by Koehler (2001) in 1996. It was not measured in the following years, missing the periastron passage in 1999. The next measurements were made only in 2008 by Vogt et al. (2012)

² <http://www.astro.yale.edu/smarts/>

³ Codebase: <http://www.ctio.noao.edu/~jatokovin/orbit/>

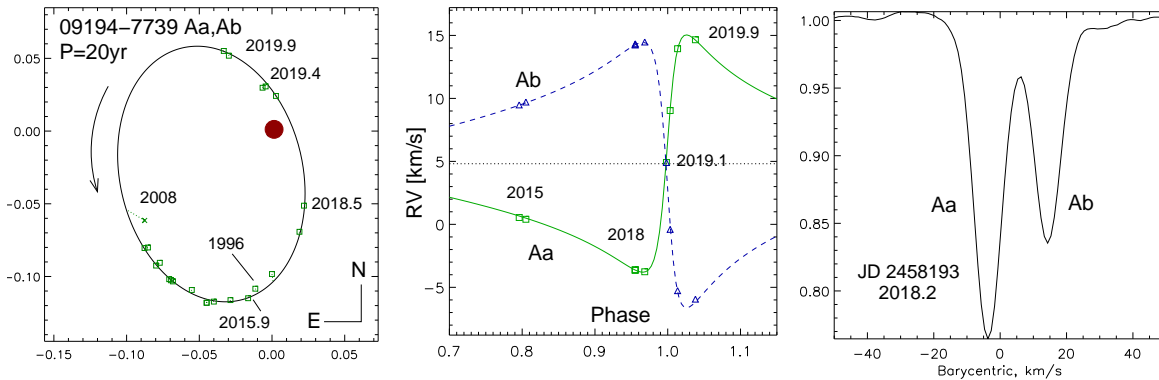


Figure 2. Visual and spectroscopic orbit of HIP 45734 Aa,Ab (KOH 83). Left: orbit in the sky (scale in arcseconds, Aa is at the coordinate origin), center: fragment of the RV curve, right: CCF in 2018.2 with two resolved dips.

Table 4
Measurements and residuals of Aa,Ab

Date (yr)	θ ($^\circ$)	ρ ($''$)	σ_ρ ($''$)	$O-C_{\theta,\rho}$ ($^\circ$)	$O-C_{\theta,\rho}$ ($''$)	Ref. ^a
1996.2420	173.9	0.1090	0.010	-1.2	-0.003	K
2008.1329	125.2	0.1070	0.050	6.7	-0.007	V
2010.0841	133.3	0.1170	0.010	0.5	-0.002	T
2010.0841	132.7	0.1190	0.010	-0.2	-0.000	T
2011.0353	139.4	0.1221	0.002	-0.0	0.000	S
2011.0353	139.7	0.1190	0.002	0.3	-0.003	S
2012.1003	146.8	0.1238	0.002	0.3	0.000	S
2012.1003	145.4	0.1240	0.002	-1.1	0.000	S
2012.1003	146.1	0.1239	0.002	-0.4	0.000	S
2013.1270	153.4	0.1224	0.005	0.2	-0.002	S
2014.0418	159.3	0.1264	0.002	0.2	0.002	S
2014.0418	159.4	0.1263	0.002	0.2	0.002	S
2014.3010	161.4	0.1239	0.002	0.5	0.000	S
2015.1036	166.4	0.1197	0.002	0.1	-0.001	S
2015.9117	172.1	0.1161	0.002	0.0	0.000	S
2016.9577	180.2	0.0983	0.009	-0.4	-0.005	S
2018.0850	195.5	0.0718	0.005	0.9	-0.003	S
2018.4815	203.4	0.0558	0.002	-0.4	0.000	S
2019.2099	353.9	0.0243	0.009	9.6	0.004	S
2019.3717	12.6	0.0305	0.009	4.9	-0.003	S
2019.3717	8.4	0.0310	0.009	0.7	-0.003	S
2019.8573	30.1	0.0597	0.002	0.6	-0.002	S
2019.9530	31.3	0.0643	0.002	-0.6	-0.001	S

^a K: Koehler (2001); V: Vogt et al. (2012); T: Tokovinin et al. (2010); S: speckle interferometry at SOAR;

Table 5
Radial Velocities of Aa,Ab

Date (JD +2400000)	V_1 (km s^{-1})	$(O-C)_1$ (km s^{-1})	V_2 (km s^{-1})	$(O-C)_2$ (km s^{-1})
57026.6730	0.54	-0.11	9.48	0.02
57093.7885	0.40	-0.09	9.71	0.06
58193.5840	-3.62	0.01	14.30	0.04
58194.5826	-3.65	-0.03	14.24	-0.02
58195.6018	-3.60	0.03	14.34	0.08
58290.5288	-3.76	0.02	14.48	0.05
58508.7680	4.91	-0.35	4.91	0.59
58546.6049	9.04	-0.10	-0.40	-0.38
58621.5882	13.95	0.04	-5.27	0.09
58800.8457	14.66	0.03	-5.94	0.23

and in 2010 by Tokovinin et al. (2010). This pair has been followed by speckle interferometry at SOAR since 2011. The first visual orbit of Aa,Ab with a period of 19.8 yr was published by Tokovinin et al. (2015); it is refined here using both 10 new position measurements and 10 RVs (Table 3). The position measurements and

their residuals are given in Table 4. All speckle measurements made at SOAR were re-examined and adjusted for slightly revised calibration parameters of each observing run, derived from wide pairs as described in Tokovinin (2018). The errors are assigned based on the data quality and used for setting weights inversely proportional to the square of errors. The weighted rms residuals from the new orbit are 1.4 mas in both directions. The orbital period is mostly constrained by the first observation in 1996 and the observations of the same orbit segment one revolution later, in 2015; the updated period is 20.1 yr (Figure 2).

The spectrum of A taken with CHIRON in 2015 had blended narrow lines of both components. In 2018 the lines separated further apart, then closed again and swapped after passing the periastron in 2019.1. The RVs of both components determined from the CHIRON spectra and their residuals to the orbit are given in Table 5. The rms residuals are 0.05 and 0.17 km s^{-1} for Aa and Ab, respectively; we set the RV errors to 0.07 and 0.15 km s^{-1} to balance the relative weights of the RV and speckle data in the combined orbit. RVs derived from the blended CCF dips in 2015 were given a lower weight by assigning the errors of 0.2 km s^{-1} .

The accurate *Gaia* DR2 parallax of the star B, 14.66 ± 0.03 mas, and the orbital elements yield the mass sum of $2.18 \pm 0.09 \mathcal{M}_\odot$. The mass sum error is mostly produced by the uncertainty of the a^3/P^2 ratio, estimated here by fitting 100 orbits where the input data are randomly perturbed by their nominal errors. This method accounts for the correlations between all elements. For example, the inclination i and the semi-major axis a are strongly correlated owing to the unfavorable orbit orientation. On the other hand, the *Gaia* parallax error does not contribute substantially to the overall mass error. The spectroscopic mass ratio $q_{\text{Aa,Ab}} = 0.894 \pm 0.007$ leads to the individual masses of 1.15 ± 0.05 and 1.03 ± 0.04 for Aa and Ab, respectively.

Independently of the trigonometric parallax, the combined spectro-interferometric orbit leads to the masses of 1.10 ± 0.04 and $0.98 \pm 0.03 \mathcal{M}_\odot$ for Aa and Ab, while the orbital parallax is 14.90 ± 0.37 mas. I adopt the masses of 1.12 and $1.0 \mathcal{M}_\odot$, compatible with both estimates within their errors. The orbital parallax agrees within its error with the *Gaia* parallax of the component B. The mass measurement from the visual orbit and *Gaia* parallax is slightly less accurate than the mass measurement from the combined orbit. If Aa,Ab were a simple binary,

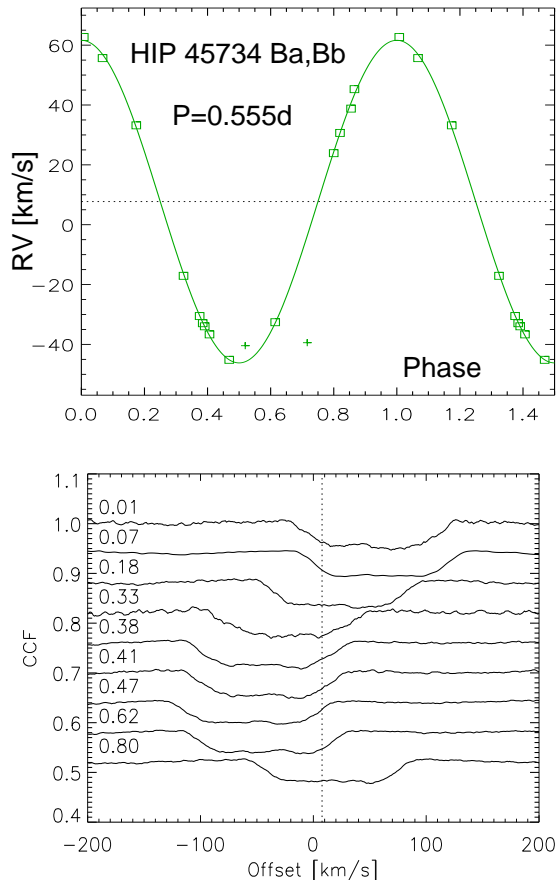


Figure 3. Radial velocity curve of the subsystem Ba,Bb (top). The lower plot shows CCF profiles ordered by the orbital phase, written near each curve; the vertical dotted line marks the systemic velocity.

rather than a quadruple, the situation would be worse because *Gaia* parallaxes of unresolved close binaries are less accurate and often biased. This will be corrected in the future *Gaia* data releases by incorporating orbital motion into the astrometric model and using ground-based measurements to extend the orbit coverage.

I compared the PM anomaly of the star A (difference between its PM measured by *Gaia* with the mean PM derived from the Hipparcos and *Gaia* positions) given by Brandt (2018), $(1.4, -0.8)$ mas yr $^{-1}$, with its value calculated from the orbit of Aa,Ab and scaled by the wobble factor $f = -0.10$ (see below), $(1.1, -0.3)$ mas yr $^{-1}$. The agreement is satisfactory, considering that the *Gaia* PMs can be biased by the orbital acceleration of A.

4. SUBSYSTEM BA,BB

4.1. Spectroscopic Orbit

The component B was considered a spectroscopic binary by Covino et al. (1997) who believed to have seen double lines. My first observation with CHIRON in 2015 (Tokovinin 2015) have shown a strange broad CCF dip with a flat bottom that resembled blended lines of two stars. However, further spectroscopic monitoring revealed that the CCF profile has a variable RV without changing its shape. Therefore, the star B is a single-lined spectroscopic binary. Some spectra of B were taken with a resolution of 30,000, sufficient for measuring the RVs.

The CHIRON RVs lead to the unique orbital solution

Table 6
Spectroscopic Orbit of Ba,Bb

Parameter	Value
Period P (day)	0.5555195 ± 0.000007
Periastron T_0 (JD)	2458195.6005 ± 0.0007
Eccentricity e	0 (fixed)
Longitude ω (deg)	0 (fixed)
Primary ampl. K_1 (km s $^{-1}$)	53.94 ± 0.43
γ velocity (km s $^{-1}$)	7.70 ± 0.28
R.M.S. residuals (km s $^{-1}$)	0.90

Table 7
Radial Velocities of Ba

Date (JD +2400000)	RV (km s $^{-1}$)	(O-C) (km s $^{-1}$)
57026.6764	23.90	-0.46
57093.7912	-32.58	0.26
57098.7099	-45.15	-0.01
58193.5867	-30.52	-0.13
58194.5861	33.21	0.73
58195.6047	62.70	1.14
58228.5560	-17.09	-0.69
58232.4904	-36.65	0.44
58284.5209	55.66	-1.23
58287.4749	-32.92	-0.26
58287.4784	-33.95	0.09
58290.5196	45.29	1.78
58546.6081	38.79	-1.92
58621.5838	30.67	0.05
58800.8497	-40.43	5.36

with $P = 0.555$ day (Figure 3 and Table 6). Approximation of the Π -shaped CCF by a Gaussian curve is poor, so the dip parameters in Table 2 derived from such approximation are inaccurate. I determined the average CCF profile and tried to fit it to each individual CCF. However, the resulting RVs were practically identical to the RVs derived by the Gaussian fits, hence I use the latter for consistency. The RVs and residuals to the orbit are given in Table 7. Despite the shallow and wide CCF, the rms residuals to the orbit are moderate, only 0.9 km s $^{-1}$; RV errors of 1 km s $^{-1}$ are assumed. This provides an indirect evidence that the secondary component Bb does not contribute to the CCF. The lower panel of Figure 3 shows CCFs of the component B ordered by the orbital phase. The CCF shape does not correlate with the phase and remains approximately constant.

Two crosses in Figure 3 denote the RV of B measured by Desidera et al. (2006) and the last CHIRON RV measured in 2019. If these RVs are used to fit the orbit, the residuals increase substantially. A small drift of the period would explain this inconsistency, although its relative value is constrained by the available CHIRON RVs to within ~ 1 ppm.

4.2. Variability

Micro-variability with the period of 0.5551 day was detected by Kiraga (2012) and attributed tentatively to the component B. Therefore, Ba rotates synchronously with the orbit. The quoted amplitude of the variability, 11 mmag in V and 27 mmag in I , refers to the combined light of A and B, hence the actual variability of B is $\sim 2.5\times$ larger. It is presumably caused by star spots.

The Transiting Exoplanet Survey Satellite (TESS,

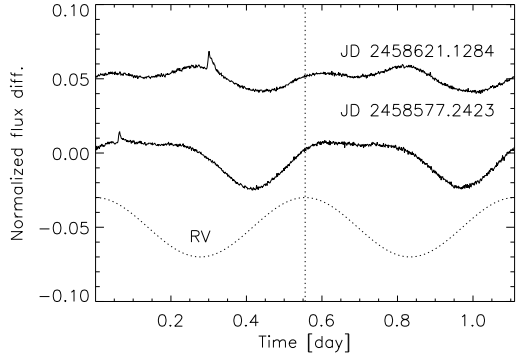


Figure 4. Two segments of TESS light curves with 2 minute cadence phased with the orbital period of Ba,Bb (0.55552 d). Julian dates of the segments’ start are indicated. The plots are displaced vertically by 0.05 to avoid overlap. The dotted cosine curve is proportional to the RV variation predicted by the orbit, with the phase zero corresponding to the RV maximum.

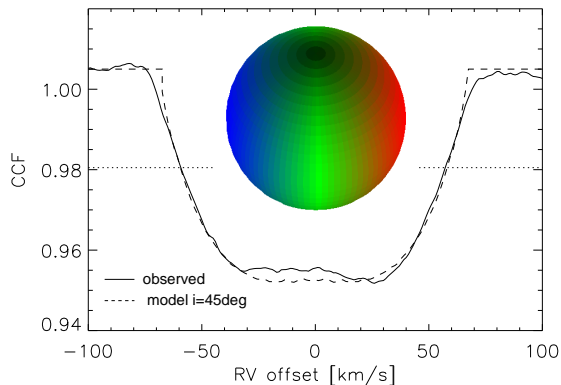


Figure 5. Average CCF of the component B (full line) and the modeled profile of a rotating star (dash) with $i = 45^\circ$ and $\alpha = 10$. The image illustrates the model of a rotating star where the color reflects the RV and the intensity depicts the polar spot without accounting for the limb darkening. The actual model has a finer grid and accounts for all effects.

Ricker et al. 2014) recently furnished accurate combined photometry of the stars A and B. I downloaded the aperture photometry of the short-cadence sequence provided by the TESS pipeline.⁴ Flux variation with the orbital period of Ba,Bb is obvious (Figure 4). Although the photometric period closely matches the orbital period, confirming the synchronous rotation of Ba, the shape of the light curve is not constant, reflecting varying distribution of spots. The variable peak to peak flux modulation corrected for the dilution by the light of A reaches almost ~ 0.1 . Spikes in the light curves show flares in the active chromosphere of Ba.

Migrating spots affect the line profile of the fast rotator Ba and contribute to the RV scatter. Note that the CCF of the component Ba (Figure 3) is slightly asymmetric, being lower on the right-hand side. This asymmetry does not change with orbital phase and could be of instrumental origin, given its sub-percent amplitude. An asymmetry should cause a systematic positive shift of the RV, biasing the measured center-of-mass velocity of Ba,Bb.

⁴ <https://mast.stsci.edu/portal/Mashup/Clients/Mast/Portal.html>

4.3. CCF Profile and Inclination

The rotation of Ba is synchronized with the orbit. The RV amplitude, CCF profile, and photometry, considered jointly, lead to the estimation of the orbital inclination $i_{\text{Ba,Bb}} = 45^\circ$ and the mass of the secondary component, $\sim 0.4 M_\odot$. First, the absolute magnitude $M_V = 5.30$ mag and the effective temperature $T_e = 5250$ K of the star B (see Section 6) allow calculation of its radius R_* as $\log R_* = 0.5 \log(L/L_\odot) - 2 \log(T_e/5777)$. With the bolometric correction of -0.24 mag appropriate for the spectral type of B, this formula gives $R_* = 1.05 R_\odot$. The Ba mass of $1 M_\odot$ is assumed because the luminosities of B and Ab are equal.

Chromospherically active binaries of RS CVn type often have “flat-bottom” line profiles when the inclination is small. Hatzes et al. (1996) explained this fact by the presence of dark polar spots. To investigate this issue, I computed the broadening function of a rotating inclined star by dividing its surface into many small zones and summing up contributions of visible zones to the line profile. A plausible quadratic limb darkening (intensity drop from 1 at the center to 0.32 at the limb) was assumed. To account for possible polar spots, my model includes the latitude intensity dependence as $1 + \alpha \cos \phi$ (ϕ is the latitude), where $\alpha > 0$ means dark polar spots and $\alpha < 0$ means polar brightening. The dashed line in Figure 5 is computed for $i = 45^\circ$ and $\alpha = 10$, i.e. $11\times$ dimmer at the pole than at the equator. The exact value of α does not matter when it is large, but small or zero values do not reproduce the “flat bottom” line profile. The model qualitatively agrees with the shape of the CCF profile. However, a small maximum at the center appears only at inclinations $i \sim 20^\circ$, which would imply an unrealistically fast equatorial speed.

The Full Width at Half Maximum (FWHM) of the CCF profile is 116 km s^{-1} . The FWHM of the modeled CCF profile equals $2 \times 0.86V \sin i$. The proportionality coefficient is almost independent of the inclination: 0.86 for $i = 35^\circ$ and $i = 45^\circ$, 0.84 for $i = 55^\circ$. Hence, $V \sin i = 58/0.86 = 67.4 \text{ km s}^{-1}$. On the other hand, the equatorial speed of a star with $R_* = 1.05 R_\odot$ and a period of 0.55 d is 94.7 km s^{-1} , therefore $i = 45^\circ$. At this inclination, the orbit gives the secondary mass of $M_{\text{Bb}} = 0.36 M_\odot$ if $M_{\text{Ba}} = 1 M_\odot$ is adopted. The mass ratio is $q_{\text{Ba,Bb}} \approx 0.4$. Large inclination implies the absence of eclipses, as observed.

Another estimate of the mass ratio, independent of orbital inclination and almost independent of the assumed mass of Ba, is obtained by comparison of the orbital and rotation speeds. For a circular orbit, the RV amplitude of the main star Ba is $K_1 = a\omega q \sin i / (1 + q)$, where $\omega = 2\pi/P$ is the angular speed and $a = 3.15 R_\odot$ is the orbital radius, computed from the third Kepler’s law for the mass sum of $1.4 M_\odot$. On the other hand, $V \sin i = R_* \omega \sin i$. The ratio of these equations gives $q/(1 + q) = (K_1/V \sin i) \times (R_*/a)$ or $q = 0.36$ after substituting the measured and estimated quantities. The agreement with the mass ratio derived from the inclination is convincing.

The CCF profile of the star B is displaced by the orbital motion by less than its full half-width. This means that some areas on the stellar surface move in anti-phase with the orbit. Indeed, in the phased CCF profiles in

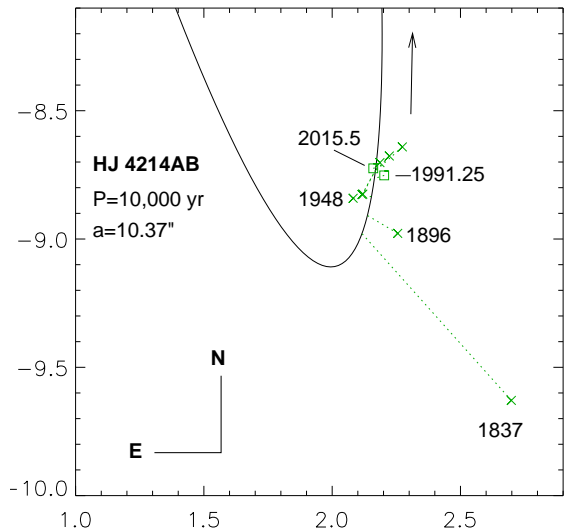


Figure 6. Selected positions of the outer pair A,B in the sky. The dates are marked; squares denote data of *Hipparcos* and *Gaia*, crosses are other measurements. Dotted lines connect measurements to the expected positions on the orbit. The line is a fragment of the tentative orbit. Axis scale in arcseconds, component A is at the coordinate origin, outside the plot.

Figure 3, the systemic RV marked by the vertical dotted line is always within the dip. The center-of-gravity of the system Ba,Bb is located inside the star Ba at a distance of $aq/(1+q) = 0.83 R_{\odot}$ from the center. Despite the short period, the close binary system is well detached. The rotation is much slower than the break-up speed of $\sim 400 \text{ km s}^{-1}$.

Spots on the rotating star Ba cause variation of its apparent RV. However, the semi-amplitude of the orbital motion, 54.93 km s^{-1} , is substantially larger than any plausible effect of the spots. Moreover, the variable spot distribution (see Figure 4) would produce an irregular and variable RV curve, while the actual RV variation is sinusoidal and coherent on a time span of several years.

5. OUTER ORBIT

The projected separation between A and B is $s = 614 \text{ au}$. If the orbit is circular and oriented face-on, s equals the semimajor axis and the third Kepler law gives a period $P^* \approx 8000 \text{ yr}$ for a mass sum of $3.5 M_{\odot}$. The orbital speed is then $2\pi s/P^* = 0.5 \text{ au yr}^{-1}$ or 2.4 km s^{-1} or 7.3 mas yr^{-1} . If the pair A,B moved with this speed, its position would have changed by $1''.3$ in 180 years elapsed since its discovery in 1837; such a displacement is measurable. In fact the pair moved much less, suggesting that the actual period might be longer and/or the apparent orbital motion in the plane of the sky is reduced by projection (Figure 6). The historical micrometer and photographic measurements recorded in the WDS have large random and systematic errors and do not help in elucidating the orbital motion of the wide pair, apart from the fact that it is substantially slower than expected for a face-on circular orbit. Modern measurements of A,B by Vogt et al. (2012) and Tokovinin et al. (2010) also appear somewhat discordant, likely because of imperfect calibration.

The most accurate measurements of the relative position of the stars A and B (where A is the photo-center of Aa,Ab) are available from *Hipparcos* and *Gaia* on a

time base of 24.25 yr. The pair has moved by -37.0 mas and $+20.4 \text{ mas}$ in the radial and tangential directions, respectively. In 2015.5 the relative position of A,B was $194''.13$ and $8''.988$. The relative positions of A,B can be described approximately by a tentative orbit ($P = 10^4 \text{ yr}$, $T = 120$, $a = 10''.4$, $e = 0.2$, $\Omega = 11''.5$, $\omega = 295^\circ$, $i = 85^\circ$). However, the orbit remains essentially unconstrained and these arbitrary elements have little value. According to this orbit, the motion is direct (position angles increase with time), but the *Hipparcos* and *Gaia* positions, after correction for precession, suggest a retrograde (clock-wise) motion.

Gaia measured accurate PMs of the stars A and B; their difference can throw some light on the motion in the wide pair. However, the orbital motion of Aa,Ab with a 20.1 yr period must be subtracted. The photo-center displacement of A is related to the relative position of Aa,Ab on its orbit by the wobble factor $f = -q/(1+q) + r/(1+r)$, where $q = 0.89$ is the mass ratio and $r = 10^{-0.4\Delta m}$ is the light ratio of Aa,Ab which depends on the wavelength. In the *V* and *K* bands, r equals 0.59 and 0.70 and f is -0.10 and -0.06 , respectively. According to the new orbit of Aa,Ab, in 2015.5 the component Ab moved on the sky relative to Aa with the velocity of $(-15.7, +3.2) \text{ mas yr}^{-1}$ in the R.A. and declination, respectively. The photo-center velocity scaled by $f = -0.10$ is $(1.6, -0.3) \text{ mas yr}^{-1}$. The difference between the PMs of A and B measured by *Gaia* is $(1.1, -2.3) \text{ mas yr}^{-1}$. Therefore, the orbital velocity of B relative to A was $(0.5, 2.0) \text{ mas yr}^{-1}$. The tentative orbit predicts relative motion of $(-0.2, 1.8) \text{ mas yr}^{-1}$. The motion in declination agrees well and matches the historic trend of decreasing angular separation between A and B (B moves to the North toward A). The smaller motion in R.A. is of opposite sign. The discrepancy could be explained if the star B had another low-mass companion with a period of a few decades. Yet, no such companion to B was found by high-contrast imaging (Asensio-Torres et al. 2018).

The measured difference between the RVs of B and A is 3 km s^{-1} , of the same order of magnitude as the expected orbital speed of A,B. However, the center-of-mass RV of B is likely biased by the asymmetry of its wide CCF, hence the measured RV difference cannot be trusted. Qualitatively, it hints that the orbital motion in the wide pair A,B is directed mostly along the line of sight, while the motion in the plane of the sky is slower, as observed.

6. PHOTOMETRY, LITHIUM, AND AGE

As the components A and B are separated by $9''$, their individual photometry is readily available. The ratio of the CCF areas of Aa and Ab leads to the magnitude difference $\Delta V_{Aa,Ab} = 0.73 \text{ mag}$ after correcting for the dependence of the line contrast on temperature. The latest speckle interferometry gives $\Delta V_{Aa,Ab} = 0.58 \text{ mag}$, which I adopt here. The differential photometry of Aa,Ab by Vogt et al. (2012) is $\Delta K_{Aa,Ab} = 0.34 \text{ mag}$, while Tokovinin et al. (2010) measured $\Delta K_{Aa,Ab} = 0.38 \text{ mag}$ and $\Delta H_{Aa,Ab} = 0.36 \text{ mag}$. Therefore, the *V* and *K* magnitude of three resolved components Aa, Ab, and B are measured. Errors of $\pm 0.02 \text{ mag}$ in the magnitude and $\pm 0.03 \text{ mag}$ in the color index are assumed.

Using the *Gaia* distance modulus $4.169 \pm 0.005 \text{ mag}$ and

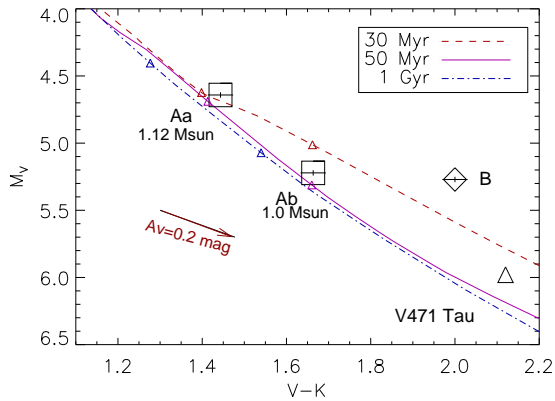


Figure 7. Location of the components Aa and Ab (squares) on the color-magnitude diagram. The lines are PARSEC isochrones (Bressan et al. 2012) for solar metallicity and ages of 30 Myr, 50 Myr, and 1 Gyr; small triangles mark the masses of 1.12 and 1.0 M_{\odot} on the isochrones. The locations of B and V471 Tau are shown by the diamond and triangle, respectively. The arrow corresponds to the interstellar extinction $A_V = 0.2$ mag.

Table 8
Parameters of components

Parameter	Aa	Ab	B
V (mag)	8.81	9.39	9.44
$V - K$ (mag)	1.44	1.66	2.00
\mathcal{M} (M_{\odot})	1.12	1.0	1.0:
T_{eff} (K)	5900	5590	5250:

assuming zero extinction, the components are placed on the color-magnitude diagram (CMD) in Figure 7. The components Aa and Ab are located very close to the main sequence. For reference, three isochrones from Bressan et al. (2012) for solar metallicity are plotted. The Dartmouth isochrones (Dotter et al. 2008) were also tested. The 1 Gyr isochrone is similar to the PARSEC one, while the 50 Myr Dartmouth isochrone does not match the data.

Table 8 gives the measured magnitudes of three resolved components, the measured masses of Aa and Ab, and the effective temperatures deduced from the $V - K$ colors and isochrones. *Gaia* gives effective temperatures of 5760 K for A (close to the average temperature derived here) and 5242 K for B. The corresponding spectral types are G0V, G6V, and K0V (Pecaut & Mamajek 2013). Curiously, *Gaia* found an extinction of 0.45 and 0.32 mag in the G band, assuming that A and B are single stars. However, there are no obvious interstellar absorptions in the spectrum of A. Given the distance of 68 pc, an average extinction of $A_V = 0.1$ mag can be expected.

The colors, absolute magnitudes, and masses of Aa and Ab match the standard values of the main-sequence stars of spectral types G0V and G6V, within the uncertainty of both the data and the isochrones. The areas of the CCF dips of Aa and Ab correspond approximately to the stars of solar metallicity. Small triangles in Figure 7 show locations of stars with the masses of Aa and Ab on the isochrones. The 50 Myr isochrone gives the best match, while at the 1 Gyr age the stars should be ~ 0.2 mag brighter than observed. However, an extinction of $A_V = 0.2$ mag would remove the discrepancy. On the other hand, the rapidly rotating star B does not conform

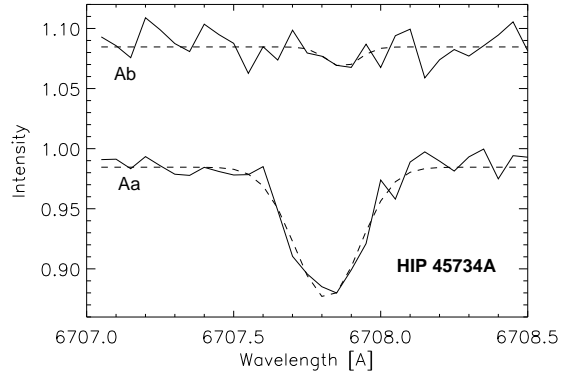


Figure 8. Profiles of the lithium lines in the components Ab (upper) and Aa (lower) are plotted by full lines, displaced vertically. The dotted lines are fitted Gaussians.

to the standard isochrones.

I do not see the 6708 Å lithium line in the spectrum of B because of its fast rotation and correspondingly low line contrast. The narrow-lined components Aa and Ab are resolved in the CHIRON spectra. Using the technique of Tokovinin (2016a), the lithium line in each component can be measured separately. Quite surprisingly, it is absent in the component Ab, but prominent in Aa (Figure 8). Its equivalent width (EW) is 30 ± 3 mÅ, less than 60 mÅ measured by Torres et al. (2006) from the unresolved spectrum of A. The component Aa contributes ~ 0.6 fraction of the flux, so the intrinsic EW of its lithium line is ~ 50 mÅ.

At the age of the Pleiades, ~ 150 Myr, stars with the masses of Aa and Ab have strong lithium lines with an EW of 120 mÅ (Soderblom et al. 1993a). In the Hyades, the EW is about 80 and 34 mÅ for stars with $B - V$ of 0.6 and 0.7 mag (Soderblom et al. 1993b). The presence of lithium in Aa and its depletion in Ab suggest that this system is substantially older than the Pleiades and maybe even older than the Hyades. However, lithium depletion depends not only on the age; this uncertainty prevents age-dating of HIP 45734 based on lithium. The isochrones in Figure 7 favor an age of ~ 50 Myr, but their dependence on metallicity and the existing uncertainty of the stellar evolutionary models preclude any firm conclusions. An interstellar extinction of 0.2 mag would place the stars Aa and Ab on the 1 Gyr isochrone. Moderate projected axial rotation of the components Aa and Ab, ~ 4 km s $^{-1}$, also suggests that these stars are not very young.

The component B (i.e the combined light of Ba and Bb) is located above the main sequence. If the small contribution of the star Bb, assumed to be an M3V dwarf, is accounted for, Ba moves in the CMD to the left by ~ 0.15 mag, but still remains above the main sequence. The characteristics of Ba,Bb are reminiscent of post common envelope binaries, where a main-sequence dwarf is paired to a white dwarf (WD). The prototypical example, V471 Tau in the Hyades, has spectral type K1V, orbital period 0 $^{\text{d}}$ 52, and a DA-type secondary component (Vaccaro et al. 2015), readily detectable in the UV. The above authors established that the mass of the red dwarf in V471 Tau is close to 1 M_{\odot} , contradicting its late spectral type and the low effective temperature of 5020 K. Obviously, this post common envelope star is

not a normal dwarf. The same may be true regarding HIP 45734B. The position of V471 Tau in the CMD is marked by the large triangle.

7. DISCUSSION

The *Gaia* distance and proper motion, together with the systemic radial velocity of A, 4.8 km s^{-1} , correspond to the heliocentric Galactic velocity vector of $(U, V, W) = (-36.1, -15.9, -12.5) \text{ km s}^{-1}$. This velocity does not match any known kinematic group of young stars in the solar neighborhood. For example, the Hyades moving group has $(U, V, W) = (-39, -18, -2) \text{ km s}^{-1}$. The object certainly belongs to the Galactic disk. Tetzlaff et al. (2011) proposed that HIP 45734 could be ejected from the Tucana-Horologium association. However, the weakly bound A,B pair would survive only if the ejection velocity were less than its orbital velocity (2 km s^{-1}), making the ejection scenario unlikely.

I looked for potential common proper motion companions in *Gaia*. All sources within 3° radius with parallax larger than 10 mas were retrieved; none matches the parallax and PM of HIP 45734. The best candidate (09:42:33.853, $-76:23:54.03$), at $1^\circ 84'$ distance from HIP 45734, has a PM of $(-116.9, 65.9) \text{ mas yr}^{-1}$, parallax 11.3 mas , and $G = 18.08 \text{ mag}$, hence it is not associated.

The secondary component in the Ba,Bb system is not detected spectrally or photometrically. It could be either a low-mass dwarf of spectral type M3V or a white dwarf. In the latter case, the short orbital period of Ba,Bb is a result of the common envelope evolution, like in the prototypical binary V471 Tau (Vacarro et al. 2015). Another recent example of such object is Wolf 1130 (HIP 98906), where a late-M type subdwarf is paired with an unusually massive WD on a 0.5 day orbit (Mace et al. 2018). Old post common envelope binaries are chromospherically active and often masquerade as young stars. If the component Bb is a WD, it could be detected in the UV. In the *Galex* image of HIP 45734 (wavelength $0.231 \mu\text{m}$), the southern star B is brighter than the star A. However, chromospherically active stars are also strong UV and x-ray emitters. In short, the nature of the star Bb remains unknown.

HIP 45734 is an excellent illustration of errors that could be made if the multiplicity were ignored or overlooked. A close binary Ba,Bb has a fast rotation and an active chromosphere and can be mistaken for a young single star. An unrecognized close unresolved pair Aa,Ab falsifies determination of stellar parameters using standard relations (e.g. in the TESS input catalog), while its *Gaia* parallax is possibly biased. A wide binary A,B with a relative motion accurately measured by *Gaia* lends itself to a dynamical analysis of its orbit, but in fact its motion is strongly biased by the subsystem and the estimated components' masses are also wrong if they are deemed to be simple stars.

This multiple system is less interesting than originally thought. It is certainly not a PMS object and is possibly older than the Hyades, although still younger than a typical age of the Galactic disk.

I thank the operators of the 1.5-m telescope for executing observations of this program and the SMARTS team at Yale for scheduling and pipeline processing. Re-

opening of CHIRON in 2017 was largely due to the enthusiasm and energy of T. Henry. Two spectra were taken on my request by F. Walter. Comments by the anonymous Referee helped to improve the presentation.

This work used the SIMBAD service operated by Centre des Données Stellaires (Strasbourg, France), bibliographic references from the Astrophysics Data System maintained by SAO/NASA, and the Washington Double Star Catalog maintained at USNO. This paper includes data collected by the TESS mission funded by the NASA Explorer Program. This work has made use of data from the European Space Agency (ESA) mission *Gaia* (<https://www.cosmos.esa.int/gaia>), processed by the *Gaia* Data Processing and Analysis Consortium (DPAC, <https://www.cosmos.esa.int/web/gaia/dpac/consortium>). Funding for the DPAC has been provided by national institutions, in particular the institutions participating in the *Gaia* Multilateral Agreement.

Facilities: CTIO:1.5m, SOAR, *Gaia*, TESS

REFERENCES

- Asensio-Torres, R., Janson, M., Bonavita, M., et al. 2018, *A&A*, 619, 43
- Brandt, T. D. 2018, *ApJS*, 239, 31
- Bressan, A., Marigo, P., Girardi, L., et al. 2012, *MNRAS*, 427, 127
- Covino, E., Alcalá, J. M., Allain, S., et al. 1997, *A&A*, 328, 187
- Desidera, S., Gratton, R. G., Lucatello, S., et al. 2006, *A&A*, 454, 553
- Dotter, A., Chaboyer, B., Jevremović, D. et al. 2008, *ApJS*, 178, 89
- Gaia* Collaboration, Brown, A. G. A., Vallenari, A., Prusti, T., et al. 2018, *A&A*, 595, 2 (Vizier Catalog I/345/gaia2).
- Hatzes, A. P., Vogt, S. S., Ramseyer, T. F. & Misch, A. 1996, *ApJ*, 469, 808
- Kiraga, M. 2012, *AcA*, 62, 67
- Koehler, R. 2001, *AJ*, 122, 3325
- Mace, G. N., Mann, A. W., Skiff, B. A., et al. 2018, *ApJ*, 854, 145
- Makarov, V. V. 2003, *AJ*, 126, 1996
- Mason, B. D., Wycoff, G. L., Hartkopf, W. I., Douglass, G. G. & Worley, C. E. 2001, *AJ*, 122, 3466
- Pecaut, M. J. & Mamajek, E. E. 2013, *ApJS*, 208, 9
- Ricker, G. R., Winn, J. N., Vanderspek, R., et al. 2014, in Society of Photo-Optical Instrumentation Engineers (SPIE) Conference Series, Vol. 9143, *Space Telescopes and Instrumentation 2014: Optical, Infrared, and Millimeter Wave*, 914320
- Soderblom, D. R., Jones, B. F., Balachandran, S., et al. 1993a, *AJ*, 106, 1059
- Soderblom, D., Pilachowski, C. A., Fedele, S. B., et al. 1993b, *AJ*, 105, 2299
- Tetzlaff, N., Neuh, R., Neuhäuser, R., & Hohle, M. M. 2011, *MNRAS*, 410, 190
- Tokovinin, A. 2014, *AJ*, 147, 87
- Tokovinin, A. 2015, *AJ*, 150, 177
- Tokovinin, A. 2016a, *AJ*, 152, 11
- Tokovinin, A. 2016b, ORBIT: IDL Software for Visual, Spectroscopic, and Combined Orbits, Zenodo, doi:10.2581/zenodo.61119
- Tokovinin, A. 2018, *PASP*, 130, 5002
- Tokovinin, A., Fischer, D. A., Bonati, M. et al. 2013, *PASP*, 125, 1336
- Tokovinin, A., Hartung, M. & Hayward, Th. L. 2010, *AJ*, 140, 510
- Tokovinin, A., Mason, B. D., Hartkopf, W. I., et al. 2015, *AJ*, 150, 50
- Tokovinin, A., Mason, B. D., Mendez, R. A., et al. 2019, *AJ*, 158, 48
- Torres, C., Quast, G. R., Da Silva, L., et al. 2006, *A&A*, 460, 695
- Vaccaro, T. R., Wilson, R. E., Van Hamme, W., et al. 2016, *ApJ*, 810, 157
- Vogt, N., Schmidt, T. O. B., Nuehauser, R. et al 2012, *A&A*, 546, 63